nuclear fusion
IAEA

PAPER • OPEN ACCESS

A kinetic line-driven radiation operator and its application to Gyrokinetics

To cite this article: Jonathan Roeltgen *et al* 2025 *Nucl. Fusion* **65** 106020

OPEN ACCESS
IOP Publishing | International Atomic Energy Agency
Nuclear Fusion
Nucl. Fusion **65** (2025) 106020 (14pp)
https://doi.org/10.1088/1741-4326/adff28

A kinetic line-driven radiation operator and its application to Gyrokinetics

Jonathan Roeltgen[1,2,*], James Juno[3], Mike Kotschenreuther[2], Tess Bernard[4], Akash Shukla[1,2], Manaure Francisquez[3], Ammar Hakim[3], Gregory Hammett[3], Dominic Power[5,6] and David Hatch[1,2]

[1] Institute for Fusion Studies, The University of Texas at Austin, Austin, TX, United States of America
[2] ExoFusion, Bellevue, WA, United States of America
[3] Princeton Plasma Physics Laboratory, Princeton, NJ, United States of America
[4] General Atomics, San Diego, CA, United States of America
[5] Blackett Lab. Plasma Physics Group, Imperial College London, London, United Kingdom of Great Britain and Northern Ireland
[6] Blackett Lab. Plasma Physics Group, Lawrence Livermore National Laboratory, Livermore, CA, United States of America

E-mail: jonathan.roeltgen@gmail.com

Received 11 April 2025, revised 21 July 2025
Accepted for publication 26 August 2025
Published 15 September 2025

Abstract

A velocity dependent, kinetic model for line radiation is developed for continuum kinetic codes. It has been implemented in the full-f gyrokinetic code Gkeyll. The total radiation for a charge state is modeled as an advection in velocity space with a form of $\nabla_v \cdot (v\nu(v)f(v))$, guaranteeing particle conservation. The velocity dependence (in the form of an effective frequency $\nu(v)$) is found through fitting the energy loss of the operator, i.e. the second velocity moment, to the radiation data in the OpenADAS database. Therefore, each individual transition does not need to be evaluated every time step, significantly reducing the computational cost of including line radiation in a kinetic model. The dependence on velocity instead of the usual, temperature, allows the radiation to be computed from non-Maxwellian electron distribution functions: We benchmark the model against a collisional radiative model using isotropic non-Maxwellian distribution functions. A velocity dependent model of radiation can more accurately describe the radiation in the more kinetic regimes expected in reactor-scale devices. The velocity dependence qualitatively captures the quantum mechanical need for a minimum velocity before any radiation occurs.

Keywords: radiation, kinetic, plasma simulation

(Some figures may appear in colour only in the online journal)

* Author to whom any correspondence should be addressed.

1. Introduction

Future reactor-scale devices, such as ITER, are expected to need a large fraction of the energy entering the Scrape-Off-Layer (SOL) dissipated to protect the target from the otherwise high heat fluxes. High heat fluxes can quickly melt the target requiring weeks or months of downtime to replace the target, rendering a fusion device economically unviable. Impurity line radiation (radiation driven by the excitation of bound electrons by impacting electrons) is a primary method to achieve the energy dissipation necessary to protect the target. For fluid codes, such as SOLPS-ITER [1], line radiation for an individual charge state can be modeled as a simple source term of the form:

$$S_\mathrm{i} = -n_\mathrm{e} n_\mathrm{i} L_\mathrm{i}\left(n_\mathrm{e}, T_\mathrm{e}\right), \tag{1}$$

where n_i is the density of the radiating charge state and $L_\mathrm{i}(n_\mathrm{e}, T_\mathrm{e})$ is the emissivity of the charge state as a function of electron density and electron temperature, respectively. The total line radiation added to the electron energy equation is then simply a sum of equation (1) over all charge states.

While this approach is sufficient for a collisional regime, reactor-scale devices, with their higher temperatures, are likely to be in a long mean free path regime in at least some fraction of the SOL where a significant portion of the radiation occurs. To better simulate plasmas in the long mean free path regime, kinetic codes are needed. However, few kinetic codes have line radiation. XGC [2] uses a fluid treatment for radiation, which is unable to account for any effects due to a non-Maxwellian distribution function. SOL-KiT [3] and BIT1 [4] have expensive operators that calculate individual transitions. Each transition is a single excitation (de-excitation) of a bound electron to a higher (lower) energy bound state caused by the collision of the atom with a free electron. Calculating individual transitions can especially become expensive when including finite-density effects where more than just the ground-state population is needed. Finite-density effects increase the required number of states and corresponding collisions that need to be simulated: indirectly increasing the computational expense. This can make even a 1D kinetic code with impurity radiation prohibitively expensive.

In this paper, we develop a semi-empirical kinetic model of line radiation for kinetic codes. It is modeled as an advection in velocity space for each individual charge state and takes into account an arbitrary number of transitions. It is then implemented in the gyrokinetic solver of the Gkeyll [5–7] code suite used to study magnetized plasmas. In section 2, the continuous form of the operator is developed for an arbitrary kinetic coordinate system, followed by section 3 which presents the discrete form in gyrokinetic coordinates. Section 4 has tests of the operator with a Maxwellian distribution that confirm the correct energy loss. In section 5 we show that the emissivity calculated using the operator agrees with a collisional-radiative model [8] even with non-Maxwellian distributions. Finally, we conclude in section 6.

2. Kinetic radiation operator

Since radiation is a collision between an atom and a free electron, it acts as a collision term $C_\mathrm{rad}[f_\mathrm{e}]$ in the Vlasov–Fokker–Planck equation for the electron probability distribution function f_e:

$$\frac{\partial f}{\partial t} + \nabla \cdot (\mathbf{v}_\mathrm{e} f_\mathrm{e}) + \nabla_v \cdot (\mathbf{a}_\mathrm{e} f_\mathrm{e}) = C_\mathrm{rad}\left[f_\mathrm{e}\right], \tag{2}$$

where $\mathbf{a}_\mathrm{e}$ is the acceleration of the electrons. This electron excitation collision integral scales as $\sim n_\mathrm{i} \mathbf{v} \sum_b \sigma_b f_\mathrm{e}$ [3, 9], where σ_b is the cross section for the bth transition, the sum is over all transitions for a charge state with density n_i, and $\mathbf{v} = \mathbf{v}_\mathrm{e} - \mathbf{v}_\mathrm{i}$ is the relative velocity between the electrons ($\mathbf{v}_\mathrm{e}$) and ions ($\mathbf{v}_\mathrm{i}$), which we assume is approximately the electron velocity. The atomic density n_i times $v\sigma$ has units of frequency. Since line radiation leads to a decrease in energy and thus speed for the electrons and conserves particles, radiation can be modeled as an advection operator in velocity space:

$$C[f_s]_\mathrm{rad} = \nabla_v \cdot \left(v \nu\left(v\right) f_\mathrm{e}\left(v\right)\right), \tag{3}$$

where $v = |\mathbf{v}|$ and $\nu(v)$ is an effective collision frequency described in section 2.1 and replaces the $n_\mathrm{i} \mathbf{v} \sum_b \sigma_b$. The second moment of equation (3) is the energy loss and needs to equal the energy loss from the fluid source, equation (1), when the distribution function is a stationary Maxwellian (f_Me). Equating these equations and taking L_i from the OpenADAS database [10] (a publicly available collection of both fundamental atomic data such as charge exchange cross sections and derived atomic data such as the emissivity) allows us to solve for $\nu(v)$:

$$\int_{-\infty}^{\infty} \frac{1}{2} m_\mathrm{e} v^2 \nabla_v \cdot \left(v \nu\left(v\right) f_\mathrm{Me}\right) \mathrm{d}v = -n_\mathrm{e} n_\mathrm{i} L_\mathrm{i}\left(n_\mathrm{e}, T_\mathrm{e}\right), \tag{4}$$

where f_Me is a Maxwellian for the electron distribution. The distribution function is assumed to be Maxwellian in equation (4), since the radiation in the OpenADAS database is calculated using quantities that assume a Maxwellian distribution. As radiation is isotropic in velocity space, we convert equation (4) to spherical coordinates. Integration by parts in spherical coordinates gives:

$$\sqrt{\frac{2 m_\mathrm{e}^5}{\pi \mathbb{e}^3}} \int_0^{\infty} \frac{v^4 \nu\left(v\right) \mathrm{e}^{-v^2 m_\mathrm{e}/(2T_\mathrm{e})}}{T_\mathrm{e}^{3/2}} \mathrm{d}v = -n_\mathrm{i} L_\mathrm{i}\left(n_\mathrm{e}, T_\mathrm{e}\right), \tag{5}$$

where $\mathbb{e}$ is the elementary charge (taken out of the temperature, which is kept in eV). As L_i's dependence on density is relatively weak for most elements (with some exceptions like Li^0), the density dependence in L_i is ignored for individual fits, and instead we calculate a different $\nu(v)$ for each electron density

within the OpenADAS database. The density dependence of $L_{\rm i}(n_{\rm e},T_{\rm e})$ is recovered by interpolating between fits with different densities (but the same atomic species and charge state) at run time. A functional form for $\nu(v)$ is assumed (detailed in the following section) whose undetermined coefficients are fitted to satisfy equation (5).

2.1. Form of $\nu(v)$

To find $\nu(v)$, a form is assumed and then equation (5) is fitted for the parameters in $\nu(v)$. Line radiation goes to 0 at low temperatures, and must also go to 0 at low velocities. It also has a minor (roughly linear) decrease at high temperatures. To accommodate these restrictions, we assume $\nu(v)$ has the following form:

$$\nu\left(v\right)=A\frac{\alpha+\beta}{\beta x^{-\alpha}+\alpha x^{\beta}}v^{\gamma}, \tag{6}$$

where $x=v/V_0$, and the fitting parameters are as follows: A, α, β, γ and V_0. The asymptotic forms of $\nu(v)$ are therefore:

$$\lim_{v\to 0}\nu\left(v\right)\propto x^{\alpha+\gamma}\text{ and }\lim_{v\to\infty}\nu\left(v\right)\propto x^{\gamma-\beta}, \tag{7}$$

with a peak radiation at $x\simeq 1$. To conserve particles and ensure the physicality of ν as v$\to 0$, the constraint $\alpha+\gamma>0$ is enforced. When integrated over a Maxwellian, the asymptotic forms of $T_{\rm e}$ are:

$$\begin{aligned}&\lim_{T_{\rm e}\to 0}\int v^4\nu\left(v\right)f_{\rm Me}\propto T_{\rm e}^{2+\alpha/2+\gamma/2}\text{ and}\\&\lim_{T_{\rm e}\to\infty}\int v^4\nu\left(v\right)f_{\rm Me}\propto T_{\rm e}^{2-\beta/2+\gamma/2}.\end{aligned} \tag{8}$$

To ensure that the energy loss of equation (3) remains finite as $v\to\infty$, the constraint $\gamma-\beta<2$ is imposed. Initial estimates of α and β can be taken from a log-log plot of the emissivity vs. temperature (such as figure 1) as the slopes at 0 and $T_{\rm e,max}$, respectively.

2.2. Variable transformation

Equation (5) is poorly scaled for computations, so we define $\bar{v}\equiv v\sqrt{m_{\rm e}/2\mathbb{e}}$ and multiply both sides by a constant ($B_s=10^{30}$), so max(L_i) ∼1. This transforms equation (5) to:

$$\sqrt{\frac{2m_{\rm e}^5}{\pi\mathbb{e}^3}}\left(2\mathbb{e}/m\right)^{(\gamma+5)/2}B_s\int_0^{\infty}\frac{\bar{v}^4\nu\left(\bar{v}\right)}{T_{\rm e}^{3/2}}{\rm e}^{-\bar{v}^2/T_{\rm e}}{\rm d}\bar{v}=n_{\rm i}L_{\rm i}B_s, \tag{9}$$

with

$$\nu\left(\bar{v}\right)=\bar{A}\frac{\alpha+\beta}{\beta x^{-\alpha}+\alpha x^{\beta}}\bar{v}^{\gamma}, \tag{10}$$

$x\equiv\frac{v}{V_0}=\frac{\bar{v}}{V_0\sqrt{m_{\rm e}/2\mathbb{e}}}$, and $\bar{A}=AC$, where A is the constant in equation (3), $\bar{A}$ is the constant from the fit, and C is a constant defined as:

$$C\equiv\frac{8\mathbb{e}}{\sqrt{\pi}n_{\rm i}}\left(\frac{2\mathbb{e}}{m_{\rm e}}\right)^{\gamma/2}. \tag{11}$$

While n_i varies in time and space, it is taken to be a constant input when fitting. It is desirable to prioritize accuracy at temperatures that have significant emissivity, so a weight w is combined with equations (9)–(11) to give the function that is minimized

$$\begin{aligned}F\left(T_{{\rm e},j},\bar{A},\alpha,\beta,\gamma,V_0\right)=\sum_j\Bigg(\Bigg[&\frac{1}{C}\int_0^{\infty}\frac{\bar{v}^4}{T_{{\rm e},j}^{3/2}}\bar{A}\frac{\alpha+\beta}{\beta x^{-\alpha}+\alpha x^{\beta}}\bar{v}^{\gamma}\\&\times{\rm e}^{-\bar{v}^2/T_{{\rm e},j}}{\rm d}\bar{v}-L_i\left(T_{{\rm e},j}\right)\Bigg]L_i\left(T_{{\rm e},j}\right)^{w-1}\Bigg)^2.\end{aligned} \tag{12}$$

With the fitting parameters found, a model emissivity $L_{\rm i,M}$, can be defined:

$$L_{\rm i,M}\left(T_{\rm e}\right)=\frac{1}{C}\int_0^{\infty}\frac{\bar{v}^4}{T_{\rm e}^{3/2}}\bar{A}\frac{\alpha+\beta}{\beta x^{-\alpha}+\alpha x^{\beta}}\bar{v}^{\gamma}{\rm e}^{-\bar{v}^2/T_{\rm e}}{\rm d}\bar{v}. \tag{13}$$

Plugging equation (10) into equation (3), the continuous operator gives:

$$\begin{aligned}&C\left[f_s\right]_{\rm rad}\\&=\frac{\bar{A}}{C}\boldsymbol{\nabla}_v\cdot\left[v\frac{\alpha+\beta}{\beta\left(\frac{v\sqrt{m_{\rm e}/2\mathbb{e}}}{V_0}\right)^{-\alpha}+\alpha\left(\frac{v\sqrt{m_{\rm e}/2\mathbb{e}}}{V_0}\right)^{\beta}}v^{\gamma}f(v)\,\hat{\mathbf{v}}\right],\end{aligned} \tag{14}$$

with fitting parameters $\bar{A}$, α, β, γ, and V_0 for each electron density and charge state and unit vector in the radial direction $\hat{\mathbf{v}}$. Fits for hydrogen and lithium are shown in figure 1. A table of the fitting parameters is given in appendix B.

3. Model equations in gyrokinetic coordinates

Gkeyll solves the full-f, long-wavelength, gyrokinetic equation using a Discontinuous Galerkin (DG) method for spatial discretization and a Runge–Kutta method for time discretization [11, 12]. The gyrokinetic equation solved for each species is:

$$\frac{\partial f_s}{\partial t}+\dot{\mathbf{R}}\cdot\nabla f_s+\dot{v_{||}}\frac{\partial f_s}{\partial v_{||}}-\nabla\cdot\left(\mathbf{D}\cdot\nabla f_s\right)=C\left[f_s\right]+S\left[f_s\right], \tag{15}$$

with $\dot{\mathbf{R}}=\{\mathbf{R},H_s\}$, $\dot{v}_{||}=\{v_{||},H_s\}$, and the gyrocenter Hamiltonian of species s is $H_s=\frac{1}{2}m_sv_{||}^2+\mu B+q_s\phi$, where ϕ is the electrostatic potential and q_s is the charge of species s. Equation (15) solves for the distribution function of species s (f_s) at the guiding center location $\mathbf{R}$, with magnetic moment $\mu=\frac{m_sv_{\perp}^2}{2B}$. $\mathbf{D}$ is an anomalous particle diffusivity typically used for radial diffusion in 2D axisymmetric cases, B is the magnetic field, and $v_{||}$ and $v_{\perp}$ are the parallel and perpendicular velocities respectively. The right-hand side $C[f_s]$ includes the different types of collisions (i.e. coulomb collisions, ionization, recombination, and radiation) and $S[f_s]$ includes other sources. Extensions to the ionization model in [13] and the recombination model are described in appendix A.

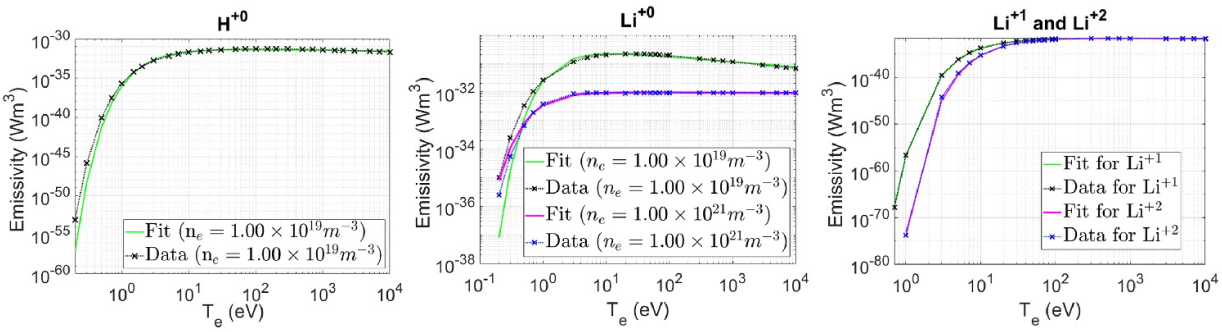

Figure 1. Select model $L_{\mathrm{i,M}}$ for hydrogen and lithium radiation with corresponding OpenADAS L_i. Li^0 has a major electron density dependence (unlike H, Li^{+1} and Li^{+2}), so individual fits are shown for several densities. Li^{+1} and Li^{+2} both have $n_\mathrm{e} = 10^{19}\,\mathrm{m}^{-3}$.

Equation (15) is coupled to the linearized gyrokinetic Poisson equation (see [6] or [7] for a more general description):

$$-\nabla_\perp \cdot \left(\frac{m_s n_{0s}}{B_0^2}\nabla_\perp \phi\right) = \sum_i q_i n_i\left(\mathbf{R}\right) - \mathrm{e}n_\mathrm{e}\left(\mathbf{R}\right), \tag{16}$$

where n_{0s} is a reference density, B_0 is a reference magnetic field, q_i and n_i are, respectively, the charge and guiding center density of ion i summed over all ions, and n_e is the guiding center electron density.

3.1. Discrete form of operator

To use equation (14) in a gyrokinetic code in $(v_{||},\mu)$ coordinates, it must first be converted to $(v_{||},\mu)$ coordinates and then discretized. Transformation from spherical to $(v_{||},\mu)$ coordinates, with corresponding unit vectors $(\hat{v}_{||},\hat{v}_\mu)$, is done with:

$$\hat{\mathbf{v}} = \frac{v_{||}}{\sqrt{v_{||}^2 + \frac{2\mu B}{m}}}\hat{v}_{||} + \frac{\sqrt{\frac{2\mu B}{m}}}{\sqrt{v_{||}^2 + \frac{2\mu B}{m}}}\hat{v}_\mu. \tag{17}$$

Equation (14) in $v_{||},\mu$ coordinates (with $v_\perp \equiv \sqrt{2\mu B/m}$) therefore is:

$$C[f_s]_\mathrm{rad} = \frac{\bar{A}}{C}\nabla_v \cdot \left[\sqrt{v_{||}^2+v_\perp^2}\,\frac{\alpha+\beta}{\beta\left(\frac{\sqrt{v_{||}^2+v_\perp^2}\sqrt{m/2\mathrm{e}}}{V_0}\right)^{-\alpha} + \alpha\left(\frac{\sqrt{v_{||}^2+v_\perp^2}\sqrt{m/2\mathrm{e}}}{V_0}\right)^{\beta}} \times \left(v_{||}^2+v_\perp^2\right)^{\gamma/2} f_\mathrm{e}\left(v_{||},\mu\right)\left(\frac{v_{||}}{\sqrt{v_{||}^2+v_\perp^2}}\hat{v}_{||} + \frac{v_\perp}{\sqrt{v_{||}^2+v_\perp^2}}\hat{v}_\mu\right)\right]. \tag{18}$$

Here, $\nabla_v\cdot$ is the divergence in $v_{||},\mu$ coordinates for some test vector $\mathbf{G}$:

$$\boldsymbol{\nabla}_v \cdot \mathbf{G} = \left[\frac{\partial G_{v_{||}}}{\partial v_{||}} + \sqrt{\frac{2m}{B}}\frac{\partial}{\partial \mu}\left(\sqrt{\mu}G_\mu\right)\right]. \tag{19}$$

For ease of notation, we define:

$$\nu'\left(v_{||},\mu\right) = v_{||}\nu\left(v_{||},\mu\right) = \frac{\bar{A}}{C}v_{||}\,\frac{\alpha+\beta}{\beta\left(\frac{\sqrt{v_{||}^2+v_\perp^2}\sqrt{m/2\mathrm{e}}}{V_0}\right)^{-\alpha} + \alpha\left(\frac{\sqrt{v_{||}^2+v_\perp^2}\sqrt{m/2\mathrm{e}}}{V_0}\right)^{\beta}} \times \left(v_{||}^2+v_\perp^2\right)^{\gamma/2}, \tag{20}$$

and

$$\nu''\left(v_{||},\mu\right) = v_\perp^2\frac{m}{B}\nu\left(v_{||},\mu\right) = \frac{\bar{A}}{C}v_\perp^2\frac{m}{B}\,\frac{\alpha+\beta}{\beta\left(\frac{\sqrt{v_{||}^2+v_\perp^2}\sqrt{m/2\mathrm{e}}}{V_0}\right)^{-\alpha} + \alpha\left(\frac{\sqrt{v_{||}^2+v_\perp^2}\sqrt{m/2\mathrm{e}}}{V_0}\right)^{\beta}} \times \left(v_{||}^2+v_\perp^2\right)^{\gamma/2}, \tag{21}$$

so equation (18) can be rewritten as:

$$C[f_s]_\mathrm{rad} = \nabla_v \cdot \left[f_\mathrm{e}\left(v_{||},\mu\right)\left(\nu'\left(v_{||},\mu\right)\hat{v}_{||} + \nu''\left(v_{||},\mu\right)\hat{v}_\mu\right)\right] \times \mathrm{d}x\mathrm{d}v_{||}\mathrm{d}\mu. \tag{22}$$

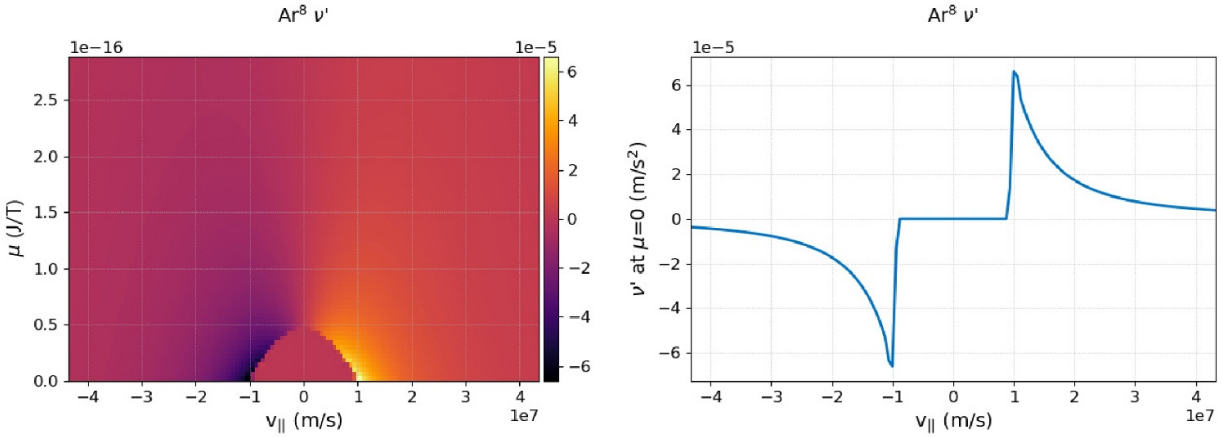

Figure 2. ν' for Ar^{+8} as both a function of μ and $v_{||}$ with $n_e = 10^{19}\,m^{-3}$ (*a*) and a slice at $\mu = 0$ (*b*). The cutoff velocity here is approximately $10^7\,m\,s^{-1}$.

The DG discretization of the operator in equation (22) follows a similar algorithm used by the drag term in the operator for elastic collisions between charged particles [14]. That is, multiply equation (22) by a test function w and integrate over a single phase-space cell $K \equiv \left[x_{i-1/2}, x_{i+1/2}\right] \times \left[v_{||j-1/2}, v_{||j+1/2}\right] \times \left[\mu_{k-1/2}, \mu_{k+1/2}\right]$ (demonstrated here using a single position dimension, x, since the generalization to 2D and 3D is trivial):

$$\int_K wC\left[f_s\right]_{\text{rad}} \mathrm{d}x\mathrm{d}v_{||}\mathrm{d}\mu \doteq \int_K w\nabla_v \cdot \left[f_e\left(v_{||},\mu\right)\left(\nu'\left(v_{||},\mu\right)\hat{v}_{||} + \nu''\left(v_{||},\mu\right)\hat{v}_\mu\right)\right] \mathrm{d}x\mathrm{d}v_{||}\mathrm{d}\mu. \quad (23)$$

Integrating equation (23) by parts, the first term on the RHS becomes:

$$\begin{aligned}&\int_K w\frac{\partial}{\partial v_{||}}\left[\nu'\left(v_{||},\mu\right)f_e\left(v_{||},\mu\right)\right]\mathrm{d}x\mathrm{d}v_{||}\mathrm{d}\mu \\ &= \int_{x_{i-1/2}}^{x_{i+1/2}}\int_{\mu_{k-1/2}}^{\mu_{k+1/2}} w\left[\nu'\left(v_{||},\mu\right)f_e\left(v_{||},\mu\right)\right]\Big|_{v_{||,j-1/2}}^{v_{||,j+1/2}} \mathrm{d}x\mathrm{d}\mu \\ &\quad - \int_K \frac{\partial w}{\partial v_{||}}\left[\nu'\left(v_{||},\mu\right)f_e\left(v_{||},\mu\right)\right]\mathrm{d}x\mathrm{d}v_{||}\mathrm{d}\mu, \end{aligned} \quad (24)$$

and the second term becomes:

$$\begin{aligned}&\int_K w\frac{\partial}{\partial \mu}\left[\nu''\left(v_{||},\mu\right)f_e\left(v_{||},\mu\right)\right]\mathrm{d}x\mathrm{d}v_{||}\mathrm{d}\mu \\ &= \int_{x_{i-1/2}}^{x_{i+1/2}}\int_{v_{||j-1/2}}^{\mu_{||j+1/2}} w\left[\nu''\left(v_{||},\mu\right)f_e\left(v_{||},\mu\right)\right]\Big|_{\mu_{k-1/2}}^{\mu_{k+1/2}} \mathrm{d}x\mathrm{d}v_{||} \\ &\quad - \int_K \frac{\partial w}{\partial \mu}\left[\nu''\left(v_{||},\mu\right)f_e\left(v_{||},\mu\right)\right]\mathrm{d}x\mathrm{d}v_{||}\mathrm{d}\mu. \end{aligned} \quad (25)$$

Due to line radiation having a cutoff velocity below which no radiation can occur, the fit parameter α is generally quite large causing ν' and ν'' to have a very large velocity gradient at the cutoff velocity, the velocity below which there is no radiation (figure 2). To handle this numerically, the velocity-dependent portion of the drag (ν'/n_i and ν''/n_i) have two separate expansions calculated at initialization: one within the volume for the volume integrals in the DG update, and one on the needed surfaces for the surface integrals. The separate surface expansions insures the continuity of the drag term even with the large velocity gradient, thus allowing us to define an upwind flux for the distribution function as in previous works utilizing DG for the kinetic equation [5–7, 15–18]. Due to this large gradient in ν' and ν'', the distribution function can steepen in the region of the cutoff velocity if the collisions are not strong enough to drive it to a Maxwellian. If the collisions are much weaker than the radiation or completely turned off, this steepening can cause numerical issues by driving parts of the distribution function negative. However, this was only observed in cases with significantly reduced collision frequencies.

Additionally, the emissivity can be negative at temperatures that are low compared to peak radiating temperatures for a species. This is due to the distribution function being largely concentrated to velocities below the cutoff velocity, figure 3. At these temperatures, the majority of the distribution has zero effect on the radiation and any negativity in the high velocity tail of the distribution function (due to the nature of the DG algorithm and collisions) has a disproportionate effect. A conservative positivity preserving algorithm (such as presented in chapter 6 in [6]) would solve this. However, in the meantime, the radiation is turned off below a cutoff temperature, which by definition has an emissivity that is nearly 3 orders of magnitude lower than the peak emissivity and so will have minimal effect on the solution.

Since different elements and charge states radiate at different temperatures, a single cutoff temperature would be insufficient. However, all elements have the same general trend of the emissivity peaking at some temperature and then rapidly dropping as the temperature decreases. This allows us to specify a cutoff temperature for each species where the emissivity is some fraction of the peak emissivity (a factor of $10^{-2.5}$ by

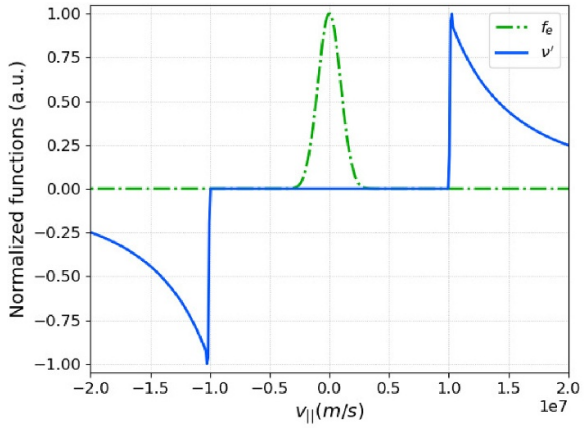

Figure 3. In blue is the ν' for Ar^{+8} at $\mu = 0$ and normalized to 1. In green is the electron distribution function at a temperature of 5 eV. The distribution function is approximately 0 in the region that $|\nu'| > 0$.

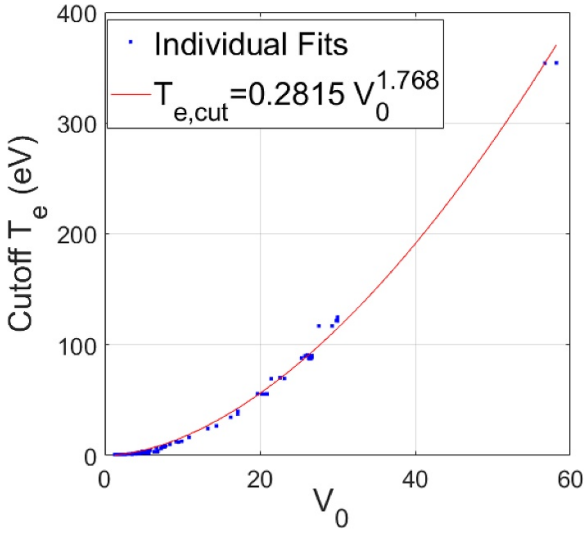

Figure 4. The temperature at which the emissivity drops by a factor of $10^{-2.5}$ from the peak emissivity as a function of the V_0 parameter (the scaled cutoff velocity). A power law is fit to this to get a cutoff temperature for an arbitrary V_0.[7]

default) and, therefore, not expected to be a significant contribution to the total radiation. The cutoff temperature is highly correlated to the V_0 fitting parameter (figure 4). Fitting a power law ($T_{e,cut} = 0.2815 \times V_0^{1.768}$ by default) to the cutoff temperature as a function of V_0 fitting parameter allows specifying a cutoff temperature for all species that simply depends on the V_0 fitting parameter.

4. Tests with Maxwellian distribution function

The verification is judged based on the operator having the correct energy loss, i.e. correct emissivity, and conserving particles. While the operator does not conserve momentum (the momentum transferred to the ions is lost), we will show in the next section that it is a negligible amount compared to the total ion momentum for most magnetized fusion parameters. To ascertain these properties, we examine the moments of the radiation operator using Maxwellian distributions below.

4.1. Moments of the radiation operator

The emissivity or energy loss converges to the correct value as the number of velocity cells increases, as shown in figure 5(*a*). At low electron temperatures and moderate (or lower) velocity resolution, the accuracy is quite poor; see the red, cyan, and black points in figure 5(*a*) below ~ 25 eV. This poor accuracy is due to the velocity grid not having sufficient resolution at and below the cutoff velocity. The cutoff velocity is the dashed line in figure 5(*b*) with $v_{||} = 0$. This is quite low compared to the maximum resolution needed to resolve several hundred eV plasmas seen in the SOL. Because DG is a higher order scheme, it is only necessary that the slope in the cell is sufficiently steep so that $\nu \approx 0$ at $v_{||} = 0$ and $\mu = 0$. Using a non-uniform spacing of the velocity cells [19], especially μ, with more cells at low velocities significantly alleviates this problem as seen by the non-uniform grid capturing the drop in emissivity at low T_e with 1/16 the cells of the coarsest uniform grid to do so (the 64×32 uniform grid). This gives a speedup of a factor of $16\times$ for the non-uniform grid compared to the 64×32 uniform grid assuming the same time step (cases with the radiation limiting the time step have not been observed but could be possible). The spacing of the μ grid is shown in figure 5(*b*), where we see that the smallest cell of the non-uniform grid is the same size as the grid with 64 cells in μ.

The operator conserves particles by design, as the integral of equation (3) is 0 from the divergence theorem, and has been verified to machine precision (not shown). Since there is a decrease in velocity and the momentum taken away by the emitted photons is negligible, there is a larger loss of momentum than is physically present. We will show that this loss in momentum is small compared to both the momentum exchange between the electrons and ions from collisions and the total momentum flux.

The momentum loss from radiation is the first moment of equation (3):

$$M_{1,\mathrm{rad}} \equiv m_e \iint v_{||} \nabla_v \cdot (\nu\nu(v) f_e(v))\, \mathrm{d}v_{||} \mathrm{d}\mu. \tag{26}$$

So long as the momentum loss from this is small compared to the collisional momentum exchange and total momentum flux it can be neglected. To calculate equation (26), we assume that $f(v)$ is a drifting Maxwellian with parallel flow velocity $u_{||}$ in the $v_{||}$ direction and numerically evaluate the integral for a range of temperatures and $u_{||}$. The collisions in Gkeyll use a Dougherty operator (LBO) discussed in [14, 15]. The momentum exchange for electron-hydrogen collisions is:

$$\frac{\partial n_e u_{||}}{\partial t} = 7.5 \times 10^4 \frac{u_{||} n_e n_i \ln\Lambda}{v_{\mathrm{th}}^3}, \tag{27}$$

[7] The two points with much higher V_0 are Ar^{+16} and Ar^{+17} which have much higher binding energy than other charge states considered.

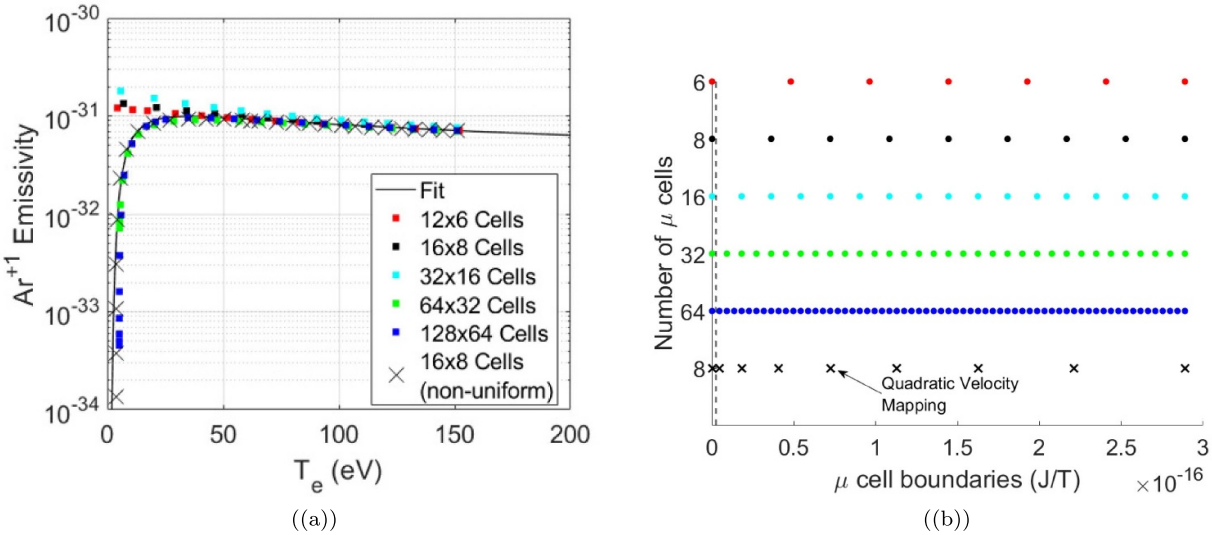

((a)) ((b))

Figure 5. In (*a*), the model emissivity $L_{\mathrm{i,M}}$ (calculated using equation (13)) is plotted along with the emissivity calculated using various velocity resolutions. All use a linear velocity grid, excepting the last (labeled non-uniform) which used a quadratic velocity mapping in both $v_{||}$ and μ. The μ cell boundaries for these different grids are shown in (*b*). It also has the cutoff velocity with $v_{||} = 0$ plotted as the dashed line.

where $\ln\Lambda$ is the Coulomb logarithm (with the density fixed at $10^{20}\,\mathrm{m}^{-3}$) and the 7.5×10^4 is from evaluating the constants in equation (2.6) in [15]. Electron-hydrogen collisions were chosen because they are generally the predominant source of momentum exchange for the electrons. We also assume $n_\mathrm{e} = n_\mathrm{H} = 10 n_\mathrm{i}$. The electron densities cancel; and, the density of radiating species (impurities or hydrogen neutrals) is typically significantly less than that of hydrogen, so a typical fraction of 10% is used. Since the radiation operator assumes $u_{||,\mathrm{i}} = 0$ (which comes from assuming $\mathbf{v_i} \approx 0$), this is also assumed for the LBO. The loss of momentum from radiation can be shown to be approximately linear in $u_{||}$ for $u_{||} \ll v_{\mathrm{th}}$, so the ratio of momentum loss to momentum exchange is approximately constant with respect to $u_{||}$. This ratio of momentum loss divided by momentum exchange is plotted in figure 6 for a range of temperatures of interest and at $u_{||} \approx c_s$. The different fits are parameterized by the V_0 fitting parameter, essentially the cutoff velocity. More tightly bound atoms with higher ionization energy have higher cutoff velocities, so higher V_0 corresponds to more tightly bound states, such as He- and Ne- like atoms. This ratio is less than 1 for all temperatures between 1 eV and 10 keV, and generally a lot less than 1 for temperatures <100 eV where most radiation occurs.

The 1D, steady state momentum equation assuming no other dissipative forces is

$$\frac{\mathrm{d}}{\mathrm{d}\ell}\left(m_\mathrm{i} u_{||,\mathrm{i}}^2 n_\mathrm{i} + n_\mathrm{i} T_\mathrm{i} + n_\mathrm{e} T_\mathrm{e}\right) = -M_{1,\mathrm{rad}}, \tag{28}$$

where m_i is the ion mass, and ℓ is the connection length. If the right-hand-side (the momentum loss) is much less than the total momentum flux (the quantity within the derivative), there is little change in the total momentum. Assuming $T_\mathrm{e} = T_\mathrm{i} = T$, $n_\mathrm{e} = n_\mathrm{i} = n$, $u_{||,\mathrm{i}} = u_{||,\mathrm{e}} = u_{||}$ and that the radiation is concentrated within a few meters (which is typical of the scrape off layer), the condition for the radiation loss to be negligible is:

$$n\left(m_\mathrm{i} u_{||}^2 + 2k_\mathrm{B}T\right) \gg -M_{1,\mathrm{rad}}. \tag{29}$$

Recalling that $M_{1,\mathrm{rad}}$ scales as n^2, a single factor of n cancels and we solve for the remaining density. This gives the maximum electron density for which the momentum flux is greater than the momentum lost from radiation. This is plotted in figure 7(*a*) for neutral hydrogen, where we see that a density greater than $10^{22}\,\mathrm{m}^{-3}$ is needed at any temperature and $u_{||}$ for the momentum loss to be comparable to the total momentum, which is not expected in magnetized fusion plasmas outside of some detached regimes where other processes (such as recombination) cause significant momentum losses.

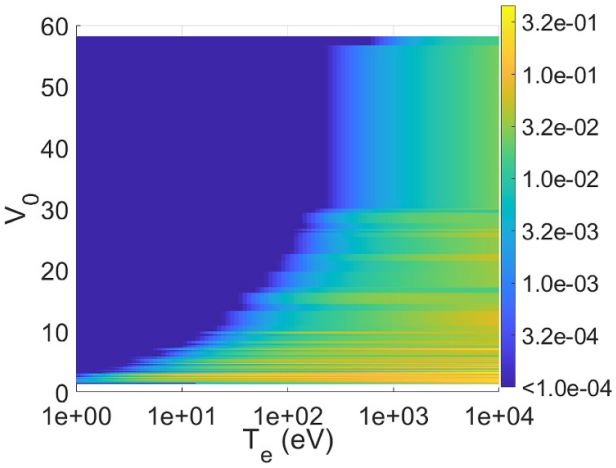

Figure 6. The radiation momentum loss (equation (26)) divided by the momentum collisional exchange (equation (27)). The *y*-axis are the different fits parameterized by the V_0 fitting parameter.

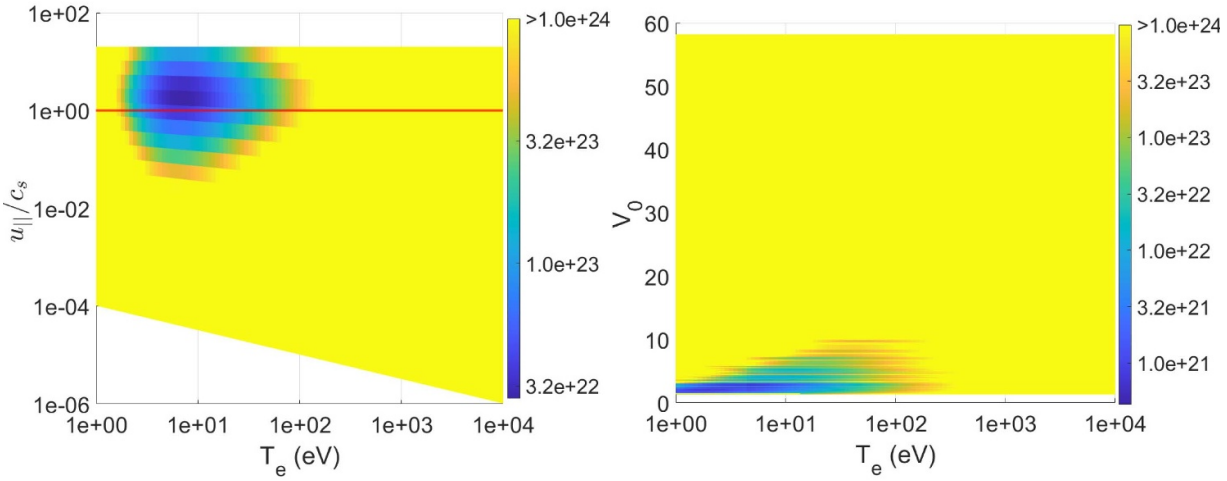

((a)) Maximum density with H^0 ((b)) Maximum density for all fits

Figure 7. Both figures (*a*) and (*b*) show the maximum density at which equation (29) is satisfied. Figure (*a*) is the maximum density that the total momentum is greater than the momentum loss for H^0. (*b*) is the maximum density that the total momentum is greater than the momentum loss at $u_{||} = c_s$ with the *y*-axis being the different fits parameterized by the V_0 fitting parameter.

In figure 7(*a*), we see that the parallel velocity where the radiation loss is largest compared to the total momentum is at approximately the sound speed c_s. So, the rest of the fits (for the remaining elements) are plotted in figure 7(*b*) as a function of temperature with $u_{||} \approx c_s$. For charge states with very low cut off velocities (represented by low V_0 fitting parameter), densities on the order of $10^{21}\,\mathrm{m}^{-3}$ can have meaningful radiation loss. However, $10^{21}\,\mathrm{m}^{-3}$ is a quite high impurity density and the charge states with low cut off velocity (i.e. Li^0, Be^0, or B^0) generally ionize very quickly as they have low binding energy. Neglecting the loss of momentum of the radiation operator is therefore a reasonable approximation as this loss is a small loss compared to both the momentum exchange and the total momentum of the system.

4.2. Coronal equilibrium

In the following, a simple flat plasma background with a trace carbon impurity is simulated and the average radiation is compared to the analytic coronal equilibrium as a simple test of the radiation in a complete simulation. We simulate every carbon charge state in a deuterium plasma with periodic boundary conditions and various electron temperatures (i.e. a separate simulation for each temperature). The carbon neutrals are static, but still act as a particle source and sink via ionization and recombination. The total carbon density is much less than the electron density and there are no energy sources or sinks other than radiation, so there is negligible energy loss (i.e. there is a constant temperature). It is then evolved until the carbon densities have reached steady state through ionization and recombination (see appendix A and [13]).

Due to the carbon being indefinitely confined and the plasma being fully ionized, the coronal equilibrium approximation is reasonable in this case. This can be found by taking the limit as $\tau_k \to \infty$ in the ionization rate equations [20]:

$$\begin{cases} n_e \left(I_{k-1} y_{k-1} - (I_k + R_k) y_k + R_{k+1} y_{k+1}\right) - \frac{y_k}{\tau_k} = 0 \\ k = 1 \ldots Z, \end{cases} \tag{30}$$

$$y_0 = 1 - \sum_{k=1}^{Z} y_k. \tag{31}$$

Here I_{k-1} are the ionization coefficients from state $k-1$ to k, R_k are the recombination coefficients from state k to $k-1$, and y_k is the fractional density of the kth charge state (the density of the kth state divided by the total density for the given element). Equation (31) says the total carbon fractional density must be 1. There is good agreement in figure 8 between the average carbon emissivity (the average emissivity of all carbon charge states weighted by the corresponding densities) and the analytic solution of the rate equations (30) and (31) for coronal equilibrium.

5. Results with non-Maxwellian distributions

The operator is benchmarked against the SIKE code [8] to examine the effects of non-Maxwellian electrons on the emissivity. The SIKE code solves the ionization/recombination rate equations (a collisional-radiative model) using an arbitrary isotropic electron distribution. This is similar to what is done to obtain the OpenADAS rates, but OpenADAS assumes a Maxwellian when calculating the rates. Since the SIKE code uses a different set of cross-sections in its calculations, fits were created specifically for this comparison from the emissivity that SIKE calculates when f is assumed to be Maxwellian. The fitting parameters are listed in table 1. Gkeyll was then run using these fits and the distribution functions calculated in [8] using SOL-KiT [3, 21]. These distributions have a predominately lower temperature population

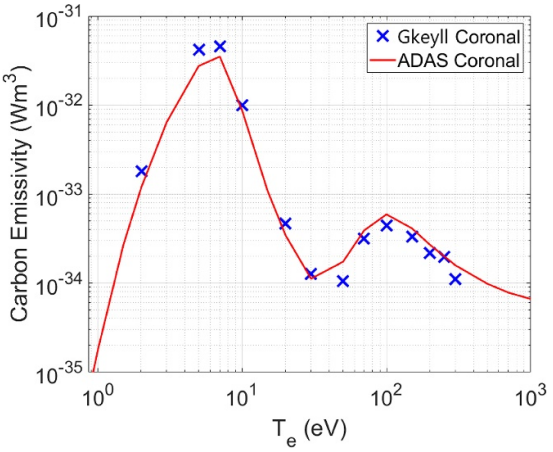

Figure 8. The average emissivity of carbon is plotted using both standard analytic equations for coronal equilibrium (solid line) and simulations to steady state with all charge states and including ionization, recombination, and radiation in Gkeyll (each point represents an individual simulation with the given electron temperature).

Table 1. Fit parameters for the Power Maxwellian emissivity (in figure 9). These parameters are also used to calculate the Gkeyll non-Maxwellian emissivity.

	A	α	β	γ	V_0
Li^0	5.671×10^{-37}	8.000×10^{03}	2.760×10^{-01}	3.008×10^{00}	1.083×10^{00}
Li^1	1.978×10^{-32}	8.000×10^{03}	4.798×10^{-01}	-9.812×10^{-01}	8.001×10^{00}
Li^2	9.913×10^{-33}	8.000×10^{03}	2.000×10^{-01}	-1.170×10^{00}	9.589×10^{00}

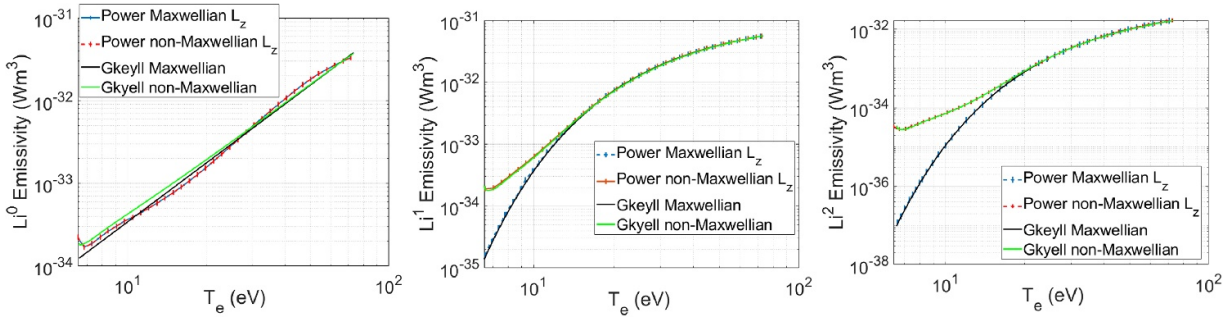

Figure 9. The emissivities of all Li charge states (Li^0 on the left, Li^{+1} in the middle, and Li^{+2} on the right) calculated using Gkeyll and the SIKE collisional radiative code. The Gkeyll emissivities here use the SIKE Maxwellian emissivity to calculate the fit parameters. The non-Maxwellian emissivities use those fitting parameters and the same distribution functions as were used in SIKE.

along with a small fraction at a hotter temperature due to non-local parallel transport in the SOL, so there is a larger fraction of high velocity electrons. This allows the emissivity for a non-Maxwellian distribution calculated by Gkeyll to be compared to the emissivity found from collisional radiative modeling (the same method used to obtain the OpenADAS data for Maxwellian distributions).

In figure 9 the emissivity for lithium from Gkeyll is plotted alongside the emissivity calculated using SIKE (figure 6 in [8]). The agreement for the non-Maxwellian Li^{+1} and Li^{+2} is exceptional, and very good for Li^0, considering the only inputs to Gkeyll are the fitting parameters found using a Maxwellian f. A selection of argon charge states with higher Z (not shown here) have similar levels of agreement as the Li^{+1} and Li^{+2}. The discrepancy between Gkeyll and Power's Maxwellian emissivity for Li^0 is simply due to the Li^0 fit being imperfect (similar to the fits not perfectly matching the data in figure 1).

While agreement of the emissivity does not guarantee that the higher moments or the change in the distribution function are correct, the emissivity is generally what is of interest. Knowing the energy loss is important for determining both the fusion performance and whether enough energy is radiated to protect the divertor target. Additionally, the exact calculation of line radiation involves many resonances that are smoothed out by the Coulomb collisions due to the resonances creating

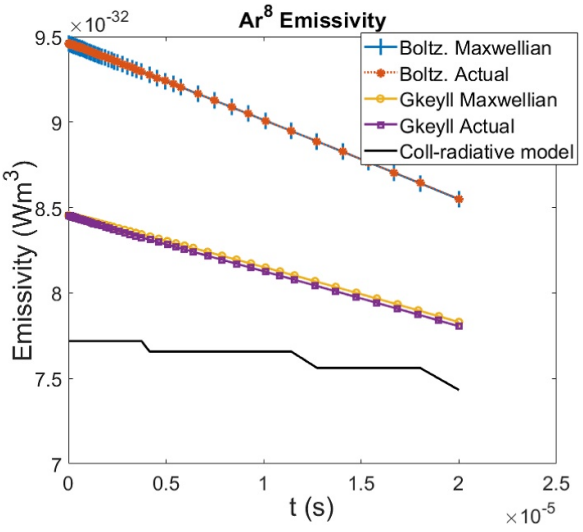

Figure 10. Emissivity from both the Boltzmann operator and equation (3) using the distribution calculated from equation (32), as well as emissivity using a Maxwellian with the same temperature for both operators. Finally, the emissivity from a collisional radiative model assuming a Maxwellian.

steep gradients. Solving for $f_e(x,v,t)$ with just Coulomb collisions and radiation:

$$\frac{\partial f_e(x,v,t)}{\partial t} = C_{\text{coll}}\left[f_e(x,v,t)\right] - C_{\text{rad}}\left[f_e(x,v,t)\right], \qquad (32)$$

the emissivity does not diverge significantly from the emissivity with a Maxwellian distribution of the same temperature which is seen in figure 10. Both equation (3) and a simplified Boltzmann collision operator for inelastic collisions were used for the radiation $C_{\text{rad}}[f_s]$, and neither diverges significantly from a Maxwellian. Specifically, the difference between the emissivity calculated with the actual distribution function (with either Gkeyll or Boltzmann operator) and the emissivity calculated using a Maxwellian of the same temperature (and same operator) is much smaller than the difference between the different models. The Coulomb collision operator is a simplification of the Fokker-Planck collision operator for isotropic distributions [3]. Both the collision operator and Boltzmann radiation are given in appendix C. This supports the conclusion in [22] that the shape of the radiation in velocity space has little effect on macroscopic quantities. Similar analyses for hydrogen, lithium, and several other argon charge states (not shown here) also show no significant difference from the Maxwellian emissivity.

6. Conclusion

A kinetic, velocity dependent operator was developed to calculate the effect of line radiation in continuum simulations. A kinetic operator allows the calculation of radiation in kinetic regimes expected in reactor-scale devices where the fluid approximation is less valid. This operator models radiation as an advection in velocity space to represent the loss of energy and guarantee particle conservation. The velocity dependence is found through fitting the energy loss of the operator to the radiation data in the OpenADAS database. This approach simplifies the calculation of line radiation computationally, so that individual transitions do not need to be calculated and it is local in velocity space.

Even 1D kinetic simulations with self-consistent impurity radiation using a Boltzmann operator would be very computationally expensive, so it is currently unknown if the kinetic description of the radiation is necessary to correctly describe the radiation profile. However, it was shown in [8] that the emissivity can change significantly due to non-local electron transport, so an efficient kinetic calculation is needed to determine how much non-local electron transport and other non-Maxwellian effects change the radiation profile. This correction to the radiation is likely to be important with edge localized modes where the high energy electrons burn through the cold detachment front and may also be important for the equilibrium radiation profiles in reactor-scale devices.

Our line radiation model was then implemented in Gkeyll, where with sufficient velocity resolution at low v the correct emissivity is obtained and it conserves particles by design. Sufficient resolution at low v is attained even at relatively low velocity resolutions with non-uniform velocity grids. The momentum loss, while larger than the actual momentum loss to the photons, is small compared to other relevant momentum rates (i.e. the momentum exchange and total momentum). Finally, the radiation emissivity was calculated using a set of non-Maxwellian electron distributions, and this emissivity matched extremely well with the emissivity found from the rate equations using these non-Maxwellian distributions. All the input files used to generate and reproduce the above results are in https://github.com/ammarhakim/gkyl-paper-inp/tree/master/2025_NF_Radiation.

Acknowledgments

This work was supported by U.S. DOE under Contract No. DEFG02-04ER54742, and the U.S. DOE Office of Fusion Energy Sciences Scientific Discovery through Advanced Computing (SciDAC) program under Award Nos. DE-SC0018429 and the CEDA SciDAC partnership DE-AC02-09CH11466. The United States Government retains a non-exclusive, paid-up, irrevocable, world-wide license to publish or reproduce the published form of this manuscript, or allow other to do so, for United States Government purposes. It also used resources of the National Energy Research Scientific Computing Center, which is supported by the Office of Science of the U.S. Department of Energy under Contract No. DE-AC02-05CH11231.

Appendix A. Ionization and recombination models

This appendix details the ionization and recombination models in Gkeyll that have been used in this work. We have extended the model of ionization presented in [13] to now include

the ionization of low-energy electrons. Secondly, our previous model did not distinguish between the impacting or scattered electron population and the ejected electrons. We now model the fact that ejected electrons may be relatively cold relative to the scattered electrons. The electron collision term is given by:

$$C_{\mathrm{e}}^{iz} = n_d \langle v_{\mathrm{e}} \sigma_{iz} \rangle \left[f_{\mathrm{e}1,M} \left(n_{\mathrm{e}}, u_{\parallel,\mathrm{e}}, v_{t,iz1}^2 \right) + f_{\mathrm{e}2,M} \left(n_{\mathrm{e}}, u_{\parallel,d}, v_{t,iz2}^2 \right) - f_{\mathrm{e}} \right], \tag{33}$$

where subscript 1 refers to the scattered electrons, and subscript 2 refers to the ejected electrons. The subscript d refers to the *donor* species (neutral or ion), which the electron impacts. The subscript M refers to the fact that Maxwellian distribution functions with the electron density, parallel flow velocity, and thermal speed are used to model the resulting electron populations. The squared thermal speeds are defined as $v_{t,iz1}^2 = T_{\mathrm{e}1}/m_{\mathrm{e}}$ and $v_{t,iz2}^2 = T_{\mathrm{e}2}/m_{\mathrm{e}}$, with the ejected electron temperature given by

$$T_{\mathrm{e}2} = \begin{cases} (1/3)\sqrt{E_{iz}\left((3/2)T_{\mathrm{e}} - E_{iz}\right)} & \text{for } (3/2)T_{\mathrm{e}} - E_{iz} > E_{iz} \\ (1/3)\left((3/2)T_{\mathrm{e}} - E_{iz}\right) & \text{for } (3/2)T_{\mathrm{e}} - E_{iz} < E_{iz}, \end{cases}$$

where E_{iz} is the ionization temperature defined in [23]. This is followed by $T_{\mathrm{e}2} = \max(T_{\mathrm{e}2}, T_{\mathrm{floor}})$ to ensure that the temperature does not drop below some limit, currently set to $T_{\mathrm{floor}} = 3\,\mathrm{eV}$. The energy of the scattered electrons is given by

$$T_{\mathrm{e}1} = \max\left(T_{\mathrm{e}} - 2E_{iz}/3 - T_{\mathrm{e}2}, T_{\mathrm{floor}}\right). \tag{34}$$

As long as the scattered and ejected electron temperatures are above T_{floor}, energy is conserved. Finally, the ionization collision terms for the resulting ion and the donor species are the same as in reference [13]. Now instead of a fitting function for the reaction rate $\langle v_{\mathrm{e}} \sigma \rangle_{iz}$, OpenADAS reaction rates are used.

Similarly, OpenADAS reaction rates are used for the recombination collision terms, which are given by:

$$C_{\mathrm{rec}}^{\mathrm{e}} = -n_{\mathrm{i}} \langle v\sigma \rangle_{\mathrm{rec}} f_{\mathrm{e}} \tag{35}$$

$$C_{\mathrm{rec}}^{\mathrm{i}} = -n_{\mathrm{e}} \langle v\sigma \rangle_{\mathrm{rec}} f_{\mathrm{i}} \tag{36}$$

$$C_{\mathrm{rec}}^{r} = n_{\mathrm{e}} \langle v\sigma \rangle_{\mathrm{rec}} f_{\mathrm{M,i}}, \tag{37}$$

where superscript r in equation (37) refers to the species that *receives* the impacting electron, either a neutral or ion. The last distribution function is a Maxwellian defined by the ion moments, reflecting the fact that this collision term may be projected on a phase-space grid different than that of the ion in equation (36).

Appendix B. Radiation fitting parameters

Fitting parameters for $Z = 1-9$ are in table 2 and $Z = \{10, 13, 18\}$ are given in table 3. All of these are for an electron density of $10^{19}\,\mathrm{m}^{-3}$. Additional fits for a few other densities (primarily Li, which has a significant density dependence unlike other elements) have been calculated and are included in the Gkeyll repository: https://github.com/ammarhakim/gkylzero.

Appendix C. Boltzmann radiation

The electron distribution function was solved for in a single cell. Solving for the radiation using the Boltzmann collision integral is more easily done with a spherical harmonic expansion of $f_{\mathrm{e}}(x, v, t)$ [3, 9]. As an inelastic collision, the pre-collision (v') and post-collision (v) velocities are related as:

$$\frac{m_{\mathrm{e}} v'^2}{2} = \frac{m_{\mathrm{e}} v^2}{2} \pm \epsilon, \tag{38}$$

where ϵ is the absolute value of the energy difference, energy gain (+) denotes de-excitations, and energy loss (-) denotes excitations. Defining

$$\alpha = v'/v = \sqrt{1 \pm \frac{2\epsilon}{m_{\mathrm{e}} v^2}}, \tag{39}$$

the integral for excitations and de-excitations can be written as

$$C[f_{\mathrm{e}}]_{\mathrm{rad}} = \sum_b n_b v \sum_{\ell,m} Y_{\ell m}(\theta, \phi) \left[\alpha^2 f_{\ell m}(\alpha v) \int_\Omega \sigma_b(\alpha v, \omega) \times P_\ell(\cos\omega)\, \mathrm{d}\Omega - f_{\ell m}(v)\, \sigma_b^{\mathrm{tot}} \right], \tag{40}$$

where the sums are over transitions b and the degree and order ℓ, m of the spherical harmonics $Y_{\ell,m}(\theta, \phi)$. The cross section of the collision is $\sigma_b(v, \omega)$, $P_n(\cos\omega)$ are the Legendre polynomials, $f_{\ell m}$ are the spherical harmonic expansions of f_{e}, $\sigma_b^{\mathrm{tot}}(v) = \int_\Omega \sigma_b(v, \omega)\mathrm{d}\Omega$, and the integrals are over the solid angle Ω. The cross sections for excitations and de-excitations between the same two states are not equal, but are related through detailed balance, described in [8]. In the case where both f_{e} and σ_b are isotropic (assumed for numerical simplification and lack of angular dependence in σ_b in the available data), equation (40) loses the angular dependence leaving only the $\ell = m = 0$ term:

$$C[f_{\mathrm{e}}]_{\mathrm{rad}} = C[f_0]_{\mathrm{rad}} = \sum_b n_b v \left[\alpha^2 f_0(\alpha v)\, \sigma_b^{\mathrm{tot}}(\alpha v) - f_0(v)\, \sigma_b^{\mathrm{tot}}(v) \right]. \tag{41}$$

The collision operator used for electron–electron collisions, again assuming an isotropic distribution, is [3]:

$$C[f_{\mathrm{e}}]_{coll} = \frac{\mathrm{e}^4 \ln\Lambda}{4\pi m_{\mathrm{e}}^2 \epsilon_0^2 v^2} \frac{\partial}{\partial v} \left[H(f_0) f_0 + D(f_0) \frac{\partial f_0}{\partial v} \right], \tag{42}$$

where ϵ_0 is the permittivity of free space, and the drag and diffusion coefficients are defined, with dummy variable u, as:

$$H(f_0) = 4\pi \int_0^v f_0(u)\, u^2 \mathrm{d}u \tag{43}$$

and

$$D(f_0) = \frac{4\pi}{v} \int_0^v u^2 \left[\int_u^\infty f_0(u')\, u' \mathrm{d}u' \right] \mathrm{d}u. \tag{44}$$

Table 2. Fitting parameters for the specified charge states of $Z < 10$. Only elements in OpenADAS have fits. All fits here are for an electron density of $10^{19}\,\mathrm{m}^{-3}$. The data comes from the OpenADAS PLT files with years: 12 for H; 96 for He, Li, Be, C, N, and O; and 89 for B and F.

Element	$\bar{A}$	α	β	γ	V_0
H^0	$5.594\,9129 \times 10^{-32}$	$8.000\,0102 \times 10^{03}$	$7.958\,7517 \times 10^{-01}$	$-1.391\,9964 \times 10^{00}$	$3.520\,1735 \times 10^{00}$
He^0	$8.012\,8134 \times 10^{-33}$	$8.000\,0011 \times 10^{03}$	$6.393\,2130 \times 10^{-01}$	$-1.035\,7297 \times 10^{00}$	$4.853\,5296 \times 10^{00}$
He^1	$4.087\,2258 \times 10^{-32}$	$8.000\,0030 \times 10^{03}$	$5.342\,7114 \times 10^{-01}$	$-1.639\,0255 \times 10^{00}$	$6.681\,0820 \times 10^{00}$
Li^0	$3.227\,6775 \times 10^{-31}$	$8.000\,0021 \times 10^{03}$	$1.631\,4718 \times 10^{00}$	$-7.228\,3424 \times 10^{-01}$	$1.831\,4244 \times 10^{00}$
Li^1	$1.839\,1597 \times 10^{-32}$	$1.5550\,315 \times 10^{04}$	$4.896\,3899 \times 10^{-01}$	$-1.480\,1717 \times 10^{00}$	$7.729\,5814 \times 10^{00}$
Li^2	$1.126\,9619 \times 10^{-32}$	$6.0237\,296 \times 10^{03}$	$8.802\,1499 \times 10^{-01}$	$-1.259\,7055 \times 10^{00}$	$9.922\,8372 \times 10^{00}$
Be^0	$1.414\,9374 \times 10^{-31}$	$8.000\,0037 \times 10^{03}$	$1.090\,2614 \times 10^{00}$	$-9.342\,6739 \times 10^{-01}$	$2.502\,4419 \times 10^{00}$
Be^1	$3.192\,1825 \times 10^{-31}$	$8.000\,0016 \times 10^{03}$	$1.242\,3977 \times 10^{00}$	$-1.201\,6297 \times 10^{00}$	$2.224\,7883 \times 10^{00}$
Be^2	$2.018\,1147 \times 10^{-32}$	$8.000\,0001 \times 10^{03}$	$4.277\,9968 \times 10^{-01}$	$-1.563\,0030 \times 10^{00}$	$1.087\,6287 \times 10^{01}$
Be^3	$2.421\,3632 \times 10^{-32}$	$8.000\,0020 \times 10^{03}$	$3.950\,7648 \times 10^{-01}$	$-1.741\,2337 \times 10^{00}$	$1.328\,4366 \times 10^{01}$
B^0	$2.7718\,200 \times 10^{-30}$	$8.000\,0047 \times 10^{03}$	$1.186\,3304 \times 10^{00}$	$-1.810\,5705 \times 10^{00}$	$2.328\,0687 \times 10^{00}$
B^1	$1.576\,6641 \times 10^{-30}$	$8.000\,0019 \times 10^{03}$	$1.093\,0601 \times 10^{00}$	$-1.856\,9471 \times 10^{00}$	$2.501\,3116 \times 10^{00}$
B^2	$5.324\,0374 \times 10^{-31}$	$8.000\,0036 \times 10^{03}$	$1.105\,6524 \times 10^{00}$	$-1.864\,1751 \times 10^{00}$	$2.478\,9349 \times 10^{00}$
B^3	$6.528\,7837 \times 10^{-31}$	$8.000\,0000 \times 10^{03}$	$4.739\,5275 \times 10^{-01}$	$-2.524\,7504 \times 10^{00}$	$1.440\,7971 \times 10^{01}$
B^4	$4.146\,5370 \times 10^{-31}$	$8.000\,0000 \times 10^{03}$	$3.591\,2960 \times 10^{-01}$	$-2.634\,9022 \times 10^{00}$	$1.622\,6743 \times 10^{01}$
C^0	$8.181\,8970 \times 10^{-32}$	$8.000\,0068 \times 10^{03}$	$9.048\,1739 \times 10^{-01}$	$-9.884\,5628 \times 10^{-01}$	$3.046\,6085 \times 10^{00}$
C^1	$1.323\,9133 \times 10^{-31}$	$8.000\,0025 \times 10^{03}$	$8.552\,5770 \times 10^{-01}$	$-1.235\,7963 \times 10^{00}$	$3.250\,9371 \times 10^{00}$
C^2	$3.201\,7747 \times 10^{-31}$	$5.934\,4048 \times 10^{01}$	$5.225\,9483 \times 10^{-01}$	$-1.756\,8709 \times 10^{00}$	$3.886\,2702 \times 10^{00}$
C^3	$2.356\,7116 \times 10^{-31}$	$2.228\,6771 \times 10^{01}$	$7.424\,4108 \times 10^{-01}$	$-1.693\,1096 \times 10^{00}$	$3.525\,9249 \times 10^{00}$
C^4	$2.422\,9179 \times 10^{-32}$	$8.000\,0009 \times 10^{03}$	$3.611\,2736 \times 10^{-01}$	$-1.824\,7065 \times 10^{00}$	$1.714\,9726 \times 10^{01}$
C^5	$1.542\,2726 \times 10^{-32}$	$1.030\,5208 \times 10^{02}$	$3.416\,6006 \times 10^{-01}$	$-1.735\,3765 \times 10^{00}$	$2.085\,2939 \times 10^{01}$
N^0	$6.446\,4159 \times 10^{-32}$	$8.000\,0016 \times 10^{03}$	$8.206\,0522 \times 10^{-01}$	$-1.135\,4117 \times 10^{00}$	$3.405\,5939 \times 10^{00}$
N^1	$9.565\,2895 \times 10^{-32}$	$7.994\,5847 \times 10^{03}$	$8.190\,2737 \times 10^{-01}$	$-1.318\,3565 \times 10^{00}$	$3.631\,7888 \times 10^{00}$
N^2	$1.706\,5080 \times 10^{-31}$	$3.153\,3218 \times 10^{01}$	$6.529\,9993 \times 10^{-01}$	$-1.566\,8823 \times 10^{00}$	$4.339\,7650 \times 10^{00}$
N^3	$1.775\,2542 \times 10^{-31}$	$7.999\,9923 \times 10^{03}$	$7.305\,4205 \times 10^{-01}$	$-1.496\,6550 \times 10^{00}$	$4.007\,0324 \times 10^{00}$
N^4	$1.859\,3290 \times 10^{-31}$	$1.805\,3318 \times 10^{01}$	$6.607\,0023 \times 10^{-01}$	$-1.726\,1992 \times 10^{00}$	$4.065\,0678 \times 10^{00}$
N^5	$3.900\,5601 \times 10^{-32}$	$8.000\,0005 \times 10^{03}$	$3.357\,4611 \times 10^{-01}$	$-1.862\,4869 \times 10^{00}$	$2.145\,1022 \times 10^{01}$
N^6	$1.848\,3721 \times 10^{-32}$	$7.999\,9999 \times 10^{03}$	$3.278\,9302 \times 10^{-01}$	$-1.811\,5474 \times 10^{00}$	$2.314\,8852 \times 10^{01}$
O^0	$1.290\,3005 \times 10^{-31}$	$1.574\,9387 \times 10^{01}$	$5.554\,3327 \times 10^{-01}$	$-1.650\,1877 \times 10^{00}$	$5.322\,9622 \times 10^{00}$
O^1	$1.181\,2697 \times 10^{-34}$	$2.664\,4504 \times 10^{01}$	$5.145\,7098 \times 10^{00}$	$2.885\,0293 \times 10^{00}$	$4.582\,6260 \times 10^{00}$
O^2	$7.311\,3156 \times 10^{-38}$	$1.278\,5834 \times 10^{01}$	$1.021\,6974 \times 10^{01}$	$8.030\,2161 \times 10^{00}$	$4.248\,2173 \times 10^{00}$
O^3	$1.534\,7701 \times 10^{-31}$	$2.450\,9620 \times 10^{01}$	$5.867\,8145 \times 10^{-01}$	$-1.602\,6097 \times 10^{00}$	$5.047\,1910 \times 10^{00}$
O^4	$1.931\,4339 \times 10^{-31}$	$2.018\,1922 \times 10^{01}$	$5.521\,4904 \times 10^{-01}$	$-1.706\,9821 \times 10^{00}$	$5.570\,0315 \times 10^{00}$
O^5	$1.437\,7183 \times 10^{-31}$	$1.534\,9851 \times 10^{01}$	$6.031\,1313 \times 10^{-01}$	$-1.752\,9083 \times 10^{00}$	$4.589\,7300 \times 10^{00}$
O^6	$3.388\,4753 \times 10^{-32}$	$8.308\,8769 \times 10^{01}$	$2.861\,5375 \times 10^{-01}$	$-1.868\,8425 \times 10^{00}$	$2.643\,0390 \times 10^{01}$
O^7	$2.696\,1891 \times 10^{-32}$	$5.240\,2961 \times 10^{06}$	$2.975\,4774 \times 10^{-01}$	$-1.940\,7818 \times 10^{00}$	$2.661\,5251 \times 10^{01}$
F^0	$6.091\,5340 \times 10^{-31}$	$8.000\,2741 \times 10^{03}$	$6.694\,7575 \times 10^{-01}$	$-2.229\,8356 \times 10^{00}$	$4.548\,6164 \times 10^{00}$
F^1	$7.944\,1774 \times 10^{-31}$	$8.011\,7950 \times 10^{03}$	$6.271\,3340 \times 10^{-01}$	$-2.363\,4978 \times 10^{00}$	$5.013\,2597 \times 10^{00}$
F^2	$7.382\,9382 \times 10^{-31}$	$3.591\,8685 \times 10^{01}$	$5.684\,2684 \times 10^{-01}$	$-2.361\,4261 \times 10^{00}$	$5.436\,0094 \times 10^{00}$
F^3	$7.201\,0957 \times 10^{-31}$	$8.234\,2030 \times 10^{03}$	$6.536\,1925 \times 10^{-01}$	$-2.243\,7535 \times 10^{00}$	$4.905\,6474 \times 10^{00}$
F^4	$7.766\,4025 \times 10^{-31}$	$8.092\,7737 \times 10^{03}$	$6.345\,9073 \times 10^{-01}$	$-2.256\,4986 \times 10^{00}$	$4.946\,1066 \times 10^{00}$
F^5	$8.404\,0965 \times 10^{-31}$	$5.682\,4290 \times 10^{01}$	$5.736\,1878 \times 10^{-01}$	$-2.292\,1355 \times 10^{00}$	$5.113\,0499 \times 10^{00}$
F^6	$4.329\,8695 \times 10^{-31}$	$8.000\,0393 \times 10^{03}$	$7.630\,6713 \times 10^{-01}$	$-2.163\,2718 \times 10^{00}$	$3.753\,6691 \times 10^{00}$
F^7	$6.797\,9378 \times 10^{-31}$	$8.000\,0001 \times 10^{03}$	$3.027\,5063 \times 10^{-01}$	$-2.686\,6809 \times 10^{00}$	$2.759\,7904 \times 10^{01}$
F^8	$3.120\,8416 \times 10^{-31}$	$8.000\,2144 \times 10^{03}$	$3.072\,0785 \times 10^{-01}$	$-2.679\,7141 \times 10^{00}$	$2.931\,1535 \times 10^{01}$

Table 3. Parameters for the specified charge states of Ne, Al, and Ar. Only elements in OpenADAS have fits. All fits here are for an electron density of $10^{19}\,\mathrm{m}^{-3}$. The data comes from the OpenADAS PLT files with years: 96 for Ne and 89 for Al and Ar.

Element	$\bar{A}$	α	β	γ	V_0
Ne^0	$1.031\,7349 \times 10^{-32}$	$8.000\,0002 \times 10^{03}$	$6.822\,3162 \times 10^{-01}$	$-1.049\,7197 \times 10^{00}$	$4.386\,6032 \times 10^{00}$
Ne^1	$1.031\,7850 \times 10^{-31}$	$8.000\,0009 \times 10^{03}$	$5.967\,7285 \times 10^{-01}$	$-1.800\,3283 \times 10^{00}$	$5.469\,8113 \times 10^{00}$
Ne^2	$1.652\,2702 \times 10^{-31}$	$2.259\,9876 \times 10^{01}$	$5.007\,8124 \times 10^{-01}$	$-1.737\,0602 \times 10^{00}$	$6.852\,0704 \times 10^{00}$
Ne^3	$5.026\,3190 \times 10^{-32}$	$8.423\,7733 \times 10^{03}$	$6.344\,5802 \times 10^{-01}$	$-1.341\,2320 \times 10^{00}$	$4.840\,9640 \times 10^{00}$
Ne^4	$1.057\,6472 \times 10^{-31}$	$1.761\,1380 \times 10^{01}$	$5.108\,2504 \times 10^{-01}$	$-1.591\,5746 \times 10^{00}$	$6.361\,5453 \times 10^{00}$
Ne^5	$1.275\,3476 \times 10^{-31}$	$1.430\,7110 \times 10^{01}$	$4.859\,0972 \times 10^{-01}$	$-1.676\,4475 \times 10^{00}$	$6.830\,9812 \times 10^{00}$
Ne^6	$4.251\,4410 \times 10^{-32}$	$1.204\,0015 \times 10^{01}$	$1.145\,1120 \times 10^{00}$	$-1.132\,0358 \times 10^{00}$	$6.669\,4867 \times 10^{00}$
Ne^7	$1.012\,3439 \times 10^{-31}$	$1.133\,2272 \times 10^{01}$	$5.190\,0549 \times 10^{-01}$	$-1.785\,2308 \times 10^{00}$	$5.665\,8331 \times 10^{00}$
Ne^8	$1.976\,5596 \times 10^{-35}$	$2.601\,7051 \times 10^{05}$	$2.089\,3776 \times 10^{00}$	$1.824\,4107 \times 10^{-01}$	$2.999\,0375 \times 10^{01}$
Ne^9	$1.000\,0000 \times 10^{-42}$	4.7653041×10^{08}	$6.084\,1058 \times 10^{00}$	$4.750\,3753 \times 10^{00}$	$3.000\,0000 \times 10^{01}$
Al^0	$5.396\,4810 \times 10^{-31}$	$8.000\,0004 \times 10^{03}$	$1.115\,7225 \times 10^{00}$	$-1.865\,3356 \times 10^{00}$	$2.456\,6479 \times 10^{00}$
Al^1	$2.720\,7138 \times 10^{-30}$	$8.000\,0002 \times 10^{03}$	$9.192\,0192 \times 10^{-01}$	$-2.080\,7987 \times 10^{00}$	$2.634\,9074 \times 10^{00}$
Al^2	$2.668\,7992 \times 10^{-30}$	$8.000\,0059 \times 10^{03}$	$7.001\,4746 \times 10^{-01}$	$-2.299\,8547 \times 10^{00}$	$4.245\,8352 \times 10^{00}$
Al^3	$1.089\,8655 \times 10^{-30}$	$8.000\,0025 \times 10^{03}$	$4.530\,3426 \times 10^{-01}$	$-2.504\,9301 \times 10^{00}$	$9.501\,5678 \times 10^{00}$
Al^4	$3.850\,4647 \times 10^{-31}$	$7.526\,9804 \times 10^{03}$	$4.832\,4027 \times 10^{-01}$	$-2.219\,0950 \times 10^{00}$	$7.915\,7009 \times 10^{00}$
Al^5	$2.449\,0006 \times 10^{-31}$	$7.062\,5922 \times 10^{01}$	$5.000\,2812 \times 10^{-01}$	$-2.0827\,413 \times 10^{00}$	$7.198\,7280 \times 10^{00}$
Al^6	$4.176\,2772 \times 10^{-40}$	$5.814\,0381 \times 10^{01}$	$1.146\,3454 \times 10^{01}$	$8.830\,5564 \times 10^{00}$	$6.369\,2490 \times 10^{00}$
Al^7	$3.429\,7410 \times 10^{-31}$	$8.000\,0169 \times 10^{03}$	$5.657\,4098 \times 10^{-01}$	$-2.114\,9969 \times 10^{00}$	$5.991\,9821 \times 10^{00}$
Al^8	$2.813\,6224 \times 10^{-33}$	$2.601\,7050 \times 10^{05}$	$3.455\,8786 \times 10^{00}$	$6.709\,6097 \times 10^{-01}$	$5.794\,9099 \times 10^{00}$
Al^9	$1.314\,9371 \times 10^{-42}$	$4.765\,3041 \times 10^{08}$	$1.632\,2431 \times 10^{01}$	$1.341\,8813 \times 10^{01}$	$5.596\,5251 \times 10^{00}$
Al^{10}	$3.890\,4281 \times 10^{-31}$	$1.243\,1935 \times 10^{04}$	$5.081\,7941 \times 10^{-01}$	$-2.366\,1619 \times 10^{00}$	$4.732\,3823 \times 10^{00}$
Ar^0	$9.817\,4142 \times 10^{-32}$	$8.000\,0005 \times 10^{03}$	$7.701\,6632 \times 10^{-01}$	$-2.226\,3461 \times 10^{00}$	$3.713\,0941 \times 10^{00}$
Ar^1	$6.129\,2192 \times 10^{-31}$	$8.000\,0235 \times 10^{03}$	$7.243\,1156 \times 10^{-01}$	$-2.219\,7470 \times 10^{00}$	$4.114\,0589 \times 10^{00}$
Ar^2	$3.000\,8645 \times 10^{-30}$	$8.000\,0416 \times 10^{03}$	$6.388\,4957 \times 10^{-01}$	$-2.312\,6033 \times 10^{00}$	$4.874\,6127 \times 10^{00}$
Ar^3	$2.086\,1232 \times 10^{-30}$	$8.000\,0423 \times 10^{03}$	$6.575\,1328 \times 10^{-01}$	$-2.230\,0004 \times 10^{00}$	$4.636\,6614 \times 10^{00}$
Ar^4	$1.851\,6579 \times 10^{-30}$	$8.000\,0423 \times 10^{03}$	$6.409\,7242 \times 10^{-01}$	$-2.244\,4754 \times 10^{00}$	$4.584\,3623 \times 10^{00}$
Ar^5	$1.697\,2427 \times 10^{-30}$	$8.000\,0430 \times 10^{03}$	$6.577\,3257 \times 10^{-01}$	$-2.289\,7722 \times 10^{00}$	$4.605\,3158 \times 10^{00}$
Ar^6	$1.321\,3647 \times 10^{-30}$	$8.000\,0434 \times 10^{03}$	$8.671\,1585 \times 10^{-01}$	$-2.123\,1459 \times 10^{00}$	$4.626\,3131 \times 10^{00}$
Ar^7	$4.289\,5363 \times 10^{-35}$	$1.073\,9759 \times 10^{09}$	$7.686\,6856 \times 10^{00}$	$4.696\,8361 \times 10^{00}$	$4.204\,4366 \times 10^{00}$
Ar^8	$5.886\,4840 \times 10^{-32}$	$1.073\,9759 \times 10^{09}$	$1.427\,2764 \times 10^{00}$	$-1.569\,6360 \times 10^{00}$	$1.712\,7784 \times 10^{01}$
Ar^9	$4.424\,8627 \times 10^{-32}$	$1.073\,9759 \times 10^{09}$	$4.645\,7943 \times 10^{-01}$	$-1.810\,9723 \times 10^{00}$	$9.202\,4049 \times 10^{00}$
Ar^{10}	$8.827\,7913 \times 10^{-32}$	$1.073\,9759 \times 10^{09}$	$4.767\,6949 \times 10^{-01}$	$-1.932\,5577 \times 10^{00}$	$8.390\,8187 \times 10^{00}$
Ar^{11}	$1.420\,5557 \times 10^{-31}$	$1.073\,9759 \times 10^{09}$	$4.968\,4078 \times 10^{-01}$	$-2.027\,0049 \times 10^{00}$	$7.717\,8086 \times 10^{00}$
Ar^{12}	$2.841\,4383 \times 10^{-31}$	$8.039\,1367 \times 10^{03}$	$3.746\,5831 \times 10^{-01}$	$-2.278\,4946 \times 10^{00}$	$7.605\,6070 \times 10^{00}$
Ar^{13}	$2.648\,1678 \times 10^{-31}$	$8.000\,0020 \times 10^{03}$	$5.022\,3297 \times 10^{-01}$	$-2.238\,8519 \times 10^{00}$	$7.371\,3566 \times 10^{00}$
Ar^{14}	$3.886\,0321 \times 10^{-31}$	$8.000\,0240 \times 10^{03}$	$5.132\,0135 \times 10^{-01}$	$-2.361\,3486 \times 10^{00}$	$7.271\,8953 \times 10^{00}$
Ar^{15}	$1.748\,7192 \times 10^{-31}$	$8.000\,0063 \times 10^{03}$	$5.749\,1512 \times 10^{-01}$	$-2.284\,7547 \times 10^{00}$	$5.845\,6604 \times 10^{00}$
Ar^{16}	$1.491\,3886 \times 10^{-36}$	$8.000\,0069 \times 10^{03}$	$3.417\,1602 \times 10^{00}$	$4.278\,5153 \times 10^{-01}$	$5.671\,9963 \times 10^{01}$
Ar^{17}	$2.945\,1302 \times 10^{-33}$	$3.755\,4636 \times 10^{06}$	$1.339\,1883 \times 10^{00}$	$-1.611\,0684 \times 10^{00}$	$5.818\,9356 \times 10^{01}$

ORCID iDs

Jonathan Roeltgen 0000-0003-2418-0221
Tess Bernard 0000-0002-7331-9704
Manaure Francisquez 0000-0002-8247-3770
Dominic Power 0000-0002-1016-0054
David Hatch 0000-0002-1625-4385

References

[1] Schneider R., Bonnin X., Borrass K., Coster D.P., Kastelewicz H., Reiter D., Rozhansky V.A. and Braams B.J. 2006 Plasma edge physics with B2-Eirene *Contrib. Plasma Phys.* **46** 3–191

[2] Stotler D., Battaglia D., Hager R., Kim K., Koskela T., Park G. and Reinke M. 2017 Kinetic neoclassical calculations of impurity radiation profiles *Nucl. Mater. Energy* **12** 1130–5

[3] Mijin S., Antony A., Militello F. and Kingham R. 2021 SOL-KiT—fully implicit code for kinetic simulation of parallel electron transport in the tokamak scrape-off layer *Comput. Phys. Commun.* **258** 107600

[4] Tskhakaya D., Matyash K., Schneider R. and Taccogna F. 2007 The particle-in-cell method *Contrib. Plasma Phys.* **47** 563–94

[5] Shi E.L. 2017 Gyrokinetic continuum simulation of turbulence in open-field-line plasmas *PhD Dissertation* Princeton University

[6] Mandell N.R. 2021 Magnetic fluctuations in gyrokinetic simulations of tokamak scrape-off layer turbulence *PhD Dissertation* Princeton University

[7] Francisquez M., Rosen M.H., Mandell N.R., Hakim A., Forest C.B. and Hammett G.W. 2023 Toward continuum gyrokinetic study of high-field mirrors *Phys. Plasmas* **30** 102504
[8] Power D., Mijin S., Verhaegh K., Militello F. and Kingham R. 2025 The impact of non-local parallel electron transport on plasma-impurity reaction rates in tokamak scrape-off layer plasmas *Plasma Phys. Control. Fusion* **67** 045030
[9] Makabe T. and Petrovic Z.L. 2014 *Plasma Electronics: Applications in Microelectronic Device Fabrication* (CRC Press)
[10] Summers H.P. 2004 The ADAS user manual (available at: www.adas.ac.uk)
[11] Shi E.L., Hammett G.W., Stoltzfus-Dueck T. and Hakim A. 2017 Gyrokinetic continuum simulation of turbulence in a straight open-field-line plasma *J. Plasma Phys.* **83** 905830304
[12] Mandell N.R., Hakim A., Hammett G.W. and Francisquez M. 2020 Electromagnetic full-f gyrokinetics in the tokamak edge with discontinuous Galerkin methods *J. Plasma Phys.* **86** 905860109
[13] Bernard T.N., Halpern F.D., Francisquez M., Mandell N.R., Juno J., Hammett G.W., Hakim A., Wilkie G.J. and Guterl J. 2022 Kinetic modeling of neutral transport for a continuum gyrokinetic code *Phys. Plasmas* **29** 052501
[14] Francisquez M., Bernard T., Mandell N., Hammett G. and Hakim A. 2020 Conservative discontinuous Galerkin scheme of a gyro-averaged Dougherty collision operator *Nucl. Fusion* **60** 096021
[15] Francisquez M., Juno J., Hakim A., Hammett G.W. and Ernst D.R. 2022 Improved multispecies Dougherty collisions *J. Plasma Phys.* **88** 905880303
[16] Juno J., Hakim A., TenBarge J., Shi E. and Dorland W. 2018 Discontinuous Galerkin algorithms for fully kinetic plasmas *J. Comput. Phys.* **353** 110–47
[17] Hakim A. and Juno J. 2020 Alias-free, matrix-free and quadrature-free discontinuous Galerkin algorithms for (plasma) kinetic equations *SC20: Int. Conf. for High Performance Computing, Networking, Storage and Analysis* (IEEE) pp 1–15
[18] Hakim A., Francisquez M., Juno J. and Hammett G.W. 2020 Conservative discontinuous Galerkin schemes for nonlinear Dougherty-Fokker-Planck collision operators *J. Plasma Phys.* **86** 905860403
[19] Francisquez M., Hakim A., Cagas P., Shukla A., Juno J. and Hammett G.W. 2024 *Nonuniform velocity grids via conservative discrete mappings in kinetic discontinuous Galerkin models* (Transport Task Force) (available at: https://conferences.union.wisc.edu/ttf/program-info/poster-presentations-2/)
[20] Mavrin A.A. 2017 Radiative cooling rates for low-Z impurities in non-coronal equilibrium state *J. Fusion Energy* **36** 161–72
[21] Power D., Mijin S., Militello F. and Kingham R.J. 2021 Ion-electron energy transfer in kinetic and fluid modelling of the tokamak scrape-off layer *Eur. Phys. J. Plus* **136** 1104
[22] Zhao M., Chankin A. and Coster D. 2017 Kinetic simulations of electron heat flux in the scrape-off layer *Nucl. Mater. Energy* **12** 819–24
[23] Voronov G. 1997 A practical fit formula for ionization rate coefficients of atoms and ions by electron impact: Z = 1–28 *At. Data Nucl. Data tables* **65** 1–35